Nanoscale

ROYAL SOCIETY OF CHEMISTRY

MINIREVIEW

View Article Online
View Journal | View Issue

Check for updates

Cite this: *Nanoscale*, 2024, **16**, 13834

Hydrogen production catalysed by atomically precise metal clusters

Tongxin Song, Xiao Cai and Yan Zhu *

Received 28th April 2024,
Accepted 17th June 2024

DOI: 10.1039/d4nr01835d

rsc.li/nanoscale

Atomically precise metal clusters that possess the exact atom number, definitive composition, and tunable geometric and electronic structures have emerged as ideal model catalysts for many important chemical processes. Recently, metal clusters have been widely used as excellent catalysts for hydrogen production to explore the relationship between the structure and catalytic properties at the atomic level. In this review, we systematically summarize the significant developments concerning metal clusters as electrocatalysts and photocatalysts for hydrogen generation. This review also puts forward the challenges and perspectives of atomically precise metal clusters in electrocatalysis and photocatalysis in the hope of providing a valuable reference for the rational design of high-performance catalysts for hydrogen production.

Published on 09 2024. Downloaded on 28-05-26 15.06.19.

1 Introduction

In recent years, the energy demand has been increasing and traditional fossil fuels have been unable to meet the current needs of society. Therefore, a lot of research studies have been conducted on the development of sustainable and clean energy sources. Hydrogen (H_2) energy is a renewable green energy carrier with a high energy density value per unit mass (120–142 MJ kg^{-1}),[1,2] which is the best alternative to conventional fossil fuels. Currently, the main methods for H_2 production include steam reforming,[3,4] coal gasification,[5,6] the natural gas method,[7,8] industrial by-products for H_2 production,[9,10] electrocatalytic[11–13] and photocatalytic water splitting[14,15] and so on. Among these H_2 production methods, electrolysis of water utilizes renewable energy to produce H_2, with low energy consumption, less greenhouse gas release during the whole preparation process, and the obtained H_2 is of high purity and low impurity content.[16–18] Photolysis of water is the direct utilization of primary solar energy for splitting water to produce H_2 with the assistance of a photocatalyst, which is simple in operation and highly efficient without the waste of energy.[19,20] Other H_2 generation methods suffer from serious pollution and environmental problems, and the low purity of the obtained H_2 makes it difficult to meet the strategic needs of sustainable development.[21] Therefore, it is necessary to design and develop high performance catalysts for electrocatalytic and photocatalytic water splitting to produce hydrogen.

Atomically precise metal clusters (including Au, Ag, Cu, Ni, *etc.*) are a class of aggregates consisting of several to hundreds of metal atoms protected by organic ligands, with resolvable geometries and a discrete electronic structure.[22,23] Since the dimensions of metal clusters are close to the Fermi energy level of metals, they exhibit molecular-like quantum size effects that are distinguishable from bulk materials.[24] With the crystal structure of metal clusters solved, metal clusters become excellent catalysts to study the relationship between structures and catalytic performances.[25,26] Although metal clusters for the studies of electrocatalysis and photocatalysis have been reported extensively in recent years,[27,28] there are very few systematic summaries based on the application of metal clusters for catalytic H_2 production, especially through electrocatalytic and photocatalytic water splitting.

In this review, we systematically summarize the advances in H_2 production catalysed by atomically precise metal clusters, including electrochemical H_2 evolution and photolysis of water. We highlight the performance of loaded clusters, unloaded pure clusters and theoretical calculations in electrochemistry. We also focus on the cases where the photocatalytic activity has been enhanced through strategies such as binding to metal oxides, surface charge modification and valence bond bridging. It is expected that this minireview will provide valuable information on atomically precise metal clusters for catalytic H_2 energy generation.

2 Electrocatalytic H_2 production

Metal clusters have been proved to exhibit excellent electrocatalytic properties in various electrochemical reactions.[29–33] In this section, we introduce recent progress on the applications of metal clusters as electrocatalysts for the hydrogen evolution reaction (HER). The HER is a half-reaction of electro-

School of Chemistry and Chemical Engineering, Nanjing University, Nanjing 210093, China

This journal is © The Royal Society of Chemistry 2024

Published on 09 2024. Downloaded on 28-05-26 15.06.19.

catalytic water splitting that occurs at the cathode and which generally follows two possible mechanisms: the Volmer–Tafel mechanism and Volmer–Heyrovsky mechanism.[34,35] In the former, a proton (H^+) attaches to the active site of the catalysts to generate M–H* and then self-combines to form H_2,[36] while in the latter M–H* bonds with free H^+ to release H_2.[37] The formation of M–H* is the limiting step for HER, so it is necessary to develop effective catalysts to enhance the HER. Generally, platinum-based nanomaterials are considered to be the most advanced electrocatalysts for HER.[38,39] But the high price and rare earth reserves limit their practical applications. It was found that Au, Ag, Cu and other metal clusters with inert H_2 evolution also display unique electrocatalytic H_2 production activity.[40–42] These metal elements feature relatively cheap prices and high earth reserves, making the study of non-platinum metal electrocatalysis even more valuable for HER.

Back in 2017, Chen's group reported atomically precise Pd clusters protected by dodecanthiols with the molecular formula $Pd_6(SC_{12}H_{25})_{12}$ (hereafter Pd_6) and investigated the HER catalytic performance of Pd_6 loaded onto activated carbon (Pd_6/AC) and its counterpart after annealing treatment at 200 °C (Pd_6/AC-V) in 0.5 M H_2SO_4 solution.[43] Fig. 1a shows the linear sweep voltammetry (LSV) curves of Pd_6/AC, Pd_6/AC-V and commercial Pt/C catalysts. It can be seen that Pd_6/AC exhibited much better catalytic activity than Pt/C, and the onset potential of annealing-treated Pd_6/AC-V was as negative as that of Pt/C. At different applied potentials, Pd_6/AC-V presented the highest mass activity (Fig. 1b). The authors attributed this to the fact that calcination treatment removed the thiol ligands on the surface of Pd clusters, exposing more catalytic sites. Unfortunately, no explanation was given in the report as to why the thiol-capped clusters exhibited superior HER activity than commercial Pt/C. In addition, Fig. 1c and d show the accelerated durability tests (ADTs) of Pd_6/AC-V and Pd_6/AC to assess their catalytic stability. The surface-clean Pd_6/AC-V displayed superior stability over the fully protected Pd_6/AC. Although the catalysts in this study were ligand-free catalysts obtained using $Pd_6(SC_{12}H_{25})_{12}$ clusters as precursors, it had given rise to a wave of research into the electrocatalytic H_2 evolution through water splitting using atomically precise metal clusters as catalysts.[44]

Also in 2017, Jin *et al.* loaded phenylethanethiol (PET) ligand-protected $Au_{25}(PET)_{18}$ (hereafter Au_{25}) onto layered MoS_2,[45] and its scanning transmission electron microscopy (STEM) image is shown in Fig. 2a, where the Au_{25}/MoS_2 composite exhibited remarkable enhanced HER activity. Fig. 2b compares the polarization curves of a blank electrode, plain MoS_2 and Au_{25}/MoS_2 with different cluster loadings in acidic electrolyte solution. The introduction of Au_{25} reduced the onset potential of the Au_{25}/MoS_2 composites by 40 mV compared with the pristine MoS_2 nanosheets, and the mass activity was more excellent with the increase of Au_{25} loading. Electrochemical impedance spectroscopy was used to evaluate

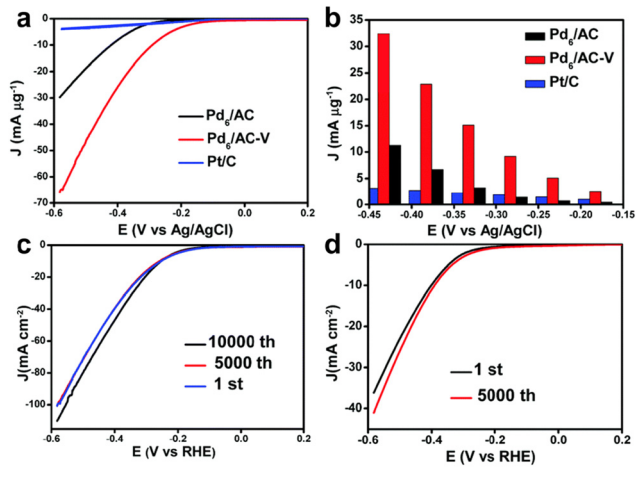

Fig. 1 (a) The polarization curves of Pd_6/AC, Pd_6/AC-V and commercial Pt/C for the HER. (b) The mass activities of the three catalysts at different applied potentials. (c) ADTs of Pd_6/AC-V. (d) ADTs of Pd_6/AC. All the LSV curves were obtained for a solution of 0.5 M H_2SO_4 with a scanning rate of 5 mV s^{-1}. Reproduced with permission from ref. 43. Copyright 2017 Royal Society of Chemistry.

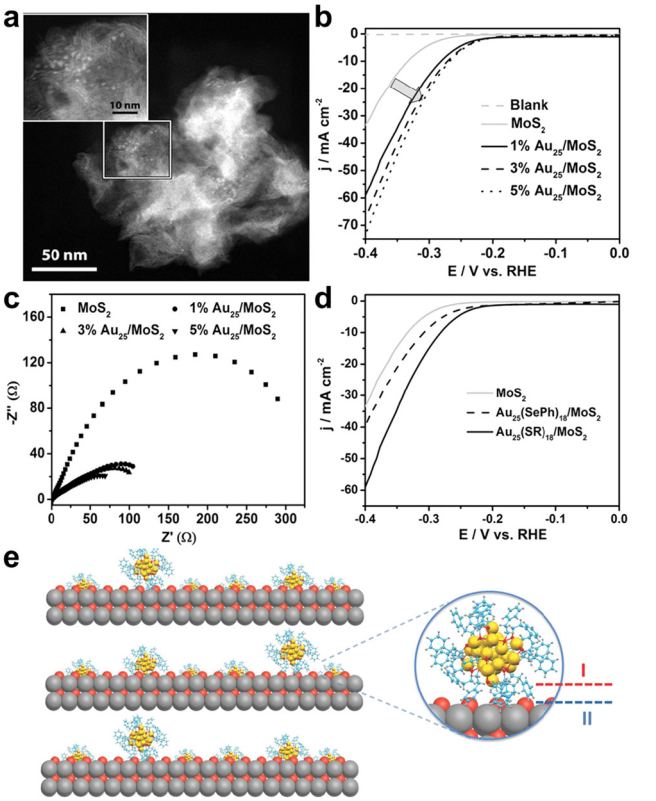

Fig. 2 (a) STEM image of $Au_{25}(PET)_{18}/MoS_2$. (b) LSV curves and (c) electrochemical impedance spectroscopy of plain MoS_2 and $Au_{25}(PET)_{18}/MoS_2$ with different loadings of composites. (d) The polarization curves of MoS_2, 1 wt% $Au_{25}(PET)_{18}/MoS_2$ and 1 wt% $Au_{25}(SePh)_{18}/MoS_2$. All the electrochemical measurements were performed in a solution of 0.5 M H_2SO_4 with a sweep rate of 5 mV s^{-1} at a rotation rate of 1600 rpm. (e) Scheme of interfacial effects of composite catalysts. Color codes: yellow = Au, red/orange = S, blue = C and gray = Mo. Reproduced with permission from ref. 45. Copyright 2017 Wiley-VCH.

Published on 09 2024. Downloaded on 28-05-26 15.06.19.

the charge transfer impedance of the catalysts, and as shown in Fig. 2c, the Au_{25}/MoS_2 catalysts exhibited smaller charge transfer impedance, indicating that the introduction of Au_{25} clusters could effectively promote charge transfer. X-ray photoelectron spectroscopy (XPS) characterization evidenced the electron transfer from Au_{25} to the MoS_2 nanosheets, implying the existence of a pronounced electronic interaction between the clusters and MoS_2 (Fig. 2e interface II), which is a major factor in promoting H_2 evolution. In addition, the HER performance of electrocatalysts with different ligands of Au_{25} loaded onto MoS_2 was investigated (Fig. 2d), and the catalytic activity of phenylselenol (PhSeH)-capped $Au_{25}(SePh)_{18}$ was much lower than that of $Au_{25}(PET)_{18}$. This was attributed to the stronger electronic relay capability of $Au_{25}(PET)_{18}$, which facilitated the interfacial electronic interactions between metal core and organic ligand (Fig. 2e interface I), thus effectively improving the HER performance. It should be noted that despite the different carbon tails of PET and PhSeH, the catalytic activity of $Au_{25}(SePh)_{18}/MoS_2$ was slightly inferior to that of $Au_{25}(PET)_{18}/MoS_2$, which had better conductivity due to the conjugation effect, suggesting that the interfacial effect, not the conductivity, was the key to the catalytic activity towards the HER. The $Au_{25}(PET)_{18}/MoS_2$ nanocomposite exhibited great catalytic durability in 1000 cycles of ADTs. This finding provided important guidance for subsequent metal cluster electrocatalysis.

Gratious *et al.* used $Au_{11}(PPh_3)_7I_3$ (PPh_3 = triphenylphosphine) as a catalyst supported on MoS_2 for electrocatalytic H_2 production.[46] They found that the interfacial interaction between the cluster and MoS_2 was due to the coordination of the metal atoms of clusters with S from MoS_2. This interfacial effect also enhanced the structural stability of clusters in supported catalysts. Similarly, Zhu *et al.* also confirmed this conclusion with the alloy clusters $Au_2Pd_6S_4(PPh_3)_4(SR)_6$ (SR stands for thiol) and found that the composite catalyst ($Au_2Pd_6S_4(PPh_3)_4(SR)_6/MoS_2$) showed more attractive electrochemical H_2 production performance compared to the single-component Au_2/MoS_2 and Pd_3/MoS_2 clusters.[47] The moderate adsorption behavior of H atom on $Au_2Pd_6S_4(PPh_3)_4(SR)_6/MoS_2$ and the electronic interactions between alloy cluster and MoS_2 contributed to the excellent catalytic activity. Other carriers in the favour of the HER had also been reported in the study of electrocatalytic production of H_2 over metal cluster-based hybrid catalysts.[48] For example, reduced graphene oxide (r-GO) as a support can improve the catalyst stability by increasing electron transfer at the interface.[49] Molybdenum selenide ($MoSe_2$) can influence the electronic structure of the catalysts and provide more catalytically active sites.[50] We summarized all cases of atomically precise metal clusters employed for electrocatalytic HER in Table 1.

In addition to composite catalysts, unloaded metal clusters provide an ideal platform for studying the catalytic performance–structure relationship as well as identifying the catalytic active sites due to their precise structures. Recent research studies have also witnessed a great development in this field. For example, Kumar *et al.* investigated the size effect for HER

Table 1 HER catalytic performances of cluster catalysts reported

Catalysts	Supports	Cluster loadings	Electrolyte	E_{Onset} (mV *vs.* RHE)	η (mV *vs.* RHE) at 10 mA cm^{-2}	j (mA cm^{-2})	Tafel slope (mV dec^{-1})	Ref.
$Pd_2Au_{36}(SR)_{24}$	Carbon black	1 mmol	1.0 M B–R buffer (pH 3)	70	—	10.9@−0.6 V	—	40
$PtAu_{24}(SR)_{18}$	Carbon black	1 mmol	1.0 M B–R buffer (pH 3)	70	—	15.3@−0.6 V	—	40
$Pd_6(SR)_{12}$	Active carbon	—	0.5 M H_2SO_4	73	—	—	220	43
$Au_{25}(SR)_{18}$	MoS_2	0.2 mg cm^{-2}	0.5 M H_2SO_4	200	280	59.3@−0.4 V	79.3	45
$Au_{11}(PPh_3)_7I_3$	MoS_2	0.1 mg cm^{-2}	0.5 M H_2SO_4	—	292	—	63	46
$Au_2Pd_6S_4(PPh_3)_4(SR)_6$	MoS_2	0.1 mg cm^{-2}	0.5 M H_2SO_4	127	232	91.0@−0.4 V	67	47
$Au_{101}(PPh_3)_{21}Cl_5$	Reduced-graphene oxide	0.177 mg cm^{-2}	0.5 M H_2SO_4	—	360	18.9@−0.4 V	148	49
$Ni_7(SR)_7$	$MoSe_2$	50 μg cm^{-2}	0.5 M H_2SO_4	106	170	142@−0.35 V	91	50
$Au_{25}(SR)_{18}^-$	—	2.55 mg cm^{-2}	0.2 M $HClO_4$	190	—	26.0@−0.7 V	—	51
$Au_{36}Ag_2(SR)_{18}$	—	0.2 mg cm^{-2}	0.5 M H_2SO_4	~100	—	19.4@−0.3 V	125	52
$NiAg_{24}(SR)_{18}$	Carbon black	2.5 nmol cm^{-2}	1.0 M KOH	50	270	55.2@−0.5 V	58	53
$Au_{24}Ag_{20}(^tBuPh\text{–}C{\equiv}C)_{24}Cl_2$	Carbon nanotube	0.2 mg cm^{-2}	0.5 M H_2SO_4	—	262	—	96	54
$Au_9Ag_9(C{\equiv}CAr^F)_{18}$	Carbon black	0.714 mg cm^{-2}	0.5 M H_2SO_4	100	274	—	99	55
$PdHCu_{11}(SR)_6(C{\equiv}CPh)_4$	—	2.7 nmol cm^{-2}	0.5 M H_2SO_4	~0	50	—	40	56
$PtHCu_{11}(SR)_6(C{\equiv}CPh)_4$	—	2.5 nmol cm^{-2}	0.5 M H_2SO_4	~0	30	—	39	57
$PtAg_{28}(S_2R)_{12}(PPh_3)_2$	—	0.2 mg cm^{-2}	0.5 M H_2SO_4	—	146	63@−0.3 V	104	62
$Au_{15}Ag_{23}(^tBuC{\equiv}C)_{18}Br_6$	Carbon black	0.714 mg cm^{-2}	0.5 M H_2SO_4	—	125	—	121	63

This journal is © The Royal Society of Chemistry 2024

Published on 09 2024. Downloaded on 28-05-26 15.06.19.

using $Au_x(PET)_y$ with different atom numbers.[51] As the cluster size decreased, the binding of Au atoms to H^+ was gradually enhanced, which facilitated the HER activity. By testing the H_2 production activity of Au_{25} with different ligands, it was found that the length of the ligand created an insulating layer between the electrode and the metal core, which increased the difficulty of electron transfer, and the π–π interactions between ligands containing benzene rings also affected the electron transfer ability, which indirectly impacted the catalytic activity. In addition, the doping effect in electrochemical H_2 generation was also studied by modelling Ag-, Cu-, and Pd-doped Au_{25} as catalysts. The results showed that the doping of heteroatoms can change the electronic structure of the cluster, which affected the adsorption energy of the surface gold atoms with H^+.

Jin and colleagues reported that $Au_{36}Ag_2(SR)_{18}$ with low ligand coverage could efficiently catalyse the HER, and identified the H adsorption site through $Au_{25}(SR)_{18}^-$ and $Au_{38}(SR)_{24}$ as counterparts.[52] Fig. 3a shows the geometries and nuclear structures of three clusters: $Au_{25}(SR)_{18}^-$ has an Au@Au_{12} core structure and exhibits a typical icosahedral configuration; $Au_{38}(SR)_{24}$ possesses an Au_2@Au_{21} core and shows a dimeric structure of two icosahedra sharing the Au_3 plane; $Au_{36}Ag_2(SR)_{18}$ is a trimeric ensemble of three icosahedra sharing the Ag_2Au_1 plane and the core structure is Au_3@$Au_{27}Ag_2$. In the acidic HER reaction, the $Au_{36}Ag_2(SR)_{18}$ cluster exhibited the lowest overpotential and the optimal current density (Fig. 3b). There was no degradation of the activity after 1000 cycles of the LSV test, indicating promising catalytic stability. Fig. 3c shows the plots of the Tafel curves of the three clusters with comparable Tafel slopes indicating their similar surface chemical states. The adsorption sites of H on the three clusters were simulated by theoretical calculation, which were all fully ligand-protected and no ligand detachment occurred. The calculation results showed that the most easily adsorbed H site is the Au atom in the kernel's shell layer, and the optimized adsorption configuration is shown in Fig. 3d. For $Au_{25}(SR)_{18}^-$, H adsorbed on the Au_{12} shell; for $Au_{38}(SR)_{24}$, H adhered to the bridge site where the two icosahedra were connected; and for $Au_{36}Ag_2(SR)_{18}$, H could be favourably attached to each exposed Au.

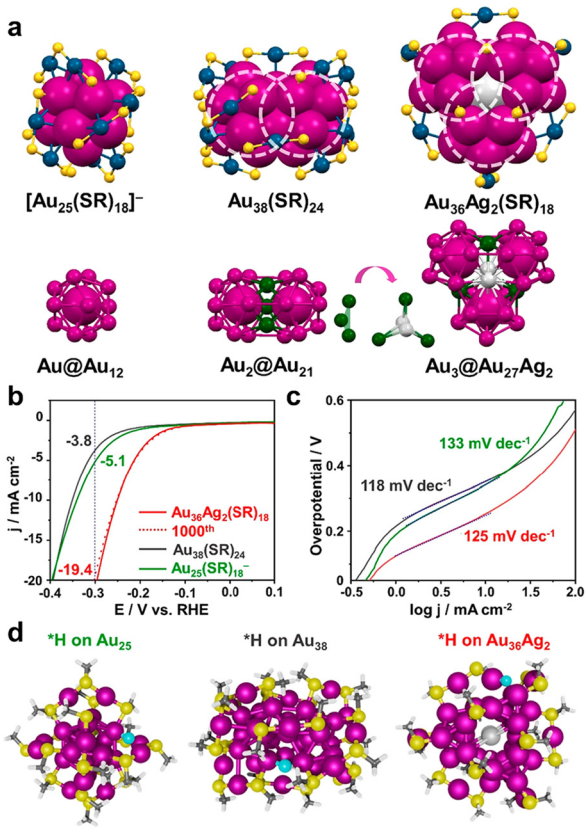

Fig. 3 (a) The geometry structures (top) and kernel structures (bottom) of $Au_{25}(SR)_{18}^-$, $Au_{38}(SR)_{24}$, and $Au_{36}Ag_2(SR)_{18}$, C with H atoms omitted; each circle indicates one icosahedral unit. (b) LSV polarization curves obtained for 0.5 M H_2SO_4 solution at a sweeping rate of 0.05 V s^{-1}. (c) Tafel plots of the three cluster catalysts. (d) The optimized adsorption structures of H on $Au_{25}(SR)_{18}^-$, $Au_{38}(SR)_{24}$, and $Au_{36}Ag_2(SR)_{18}$ clusters. Color codes: light gray = Ag, magenta/green/navy = Au, yellow = S, cyan = adsorbed H, gray = C, and white = H. Reproduced with permission from ref. 52. Copyright 2021 American Chemical Society.

Subsequently, a variety of atomically precise alloy clusters have been used for electrochemical hydrogen production, which can significantly modify the electronic structure and reduction potential due to the doping of heteroatoms, thus substantially altering the catalytic activity. For example, Lee *et al.* synthesized $Ni_1Ag_{24}(SR)_{18}$ clusters, whose HER performance far exceeded that of $Ag_{25}(SR)_{18}$ clusters.[53] Tang's group investigated the catalytic properties of AuAg alloy clusters $Au_{24}Ag_{20}(^tBuPh–C{\equiv}C)_{24}Cl_2$ and $Au_{22}Ag_{22}(^tBuC{\equiv}C)_{16}Br_{3.28}Cl_{2.72}$, which were protected with alkyne and halogen, as models for electrochemical H_2 evolution.[54] In contrast to the $Au_{36}Ag_2(SR)_{18}$ cluster mentioned previously, for the two clusters studied, H preferentially adsorbs on the Au of the staple. And the difference in catalytic performance between the two AuAg clusters originated from the two silver atoms in the core. This group also reported $Au_9Ag_9(C{\equiv}CAr^F)_{18}$ clusters as HER catalysts,[55] which displayed a unique ichthyomorphic framework. Compared with alkyne complexes of Au and Ag, the unique geometry of the $Au_9Ag_9(C{\equiv}CAr^F)_{18}$ cluster exposed more catalytic sites and therefore enhanced the catalytic activity.

Recently, H-containing 2-electron PdCu superatomic clusters were reported to offer unexpected catalytic performance for HER, which was the first example of hydride clusters applied to electrochemical H_2 production.[56] In contrast to $PdH_2Cu_{14}(SR)_6(C{\equiv}CPh)_6$ and $PdHCu_{12}(SR)_6(C{\equiv}CPh)_4$, the $PdHCu_{11}(SR)_6(C{\equiv}CPh)_4$ cluster was composed of a central Pd atom and a cuboctahedron Cu_{11} lacking a vertex with one interstitial hydride. In the case of the two former ones, the complete Cu shell layer surrounded the Pd atom in the centre, as shown in Fig. 4a, and it is worth noting that the H atom was located in the $PdCu_3$ unit. Fig. 4b shows the LSV curves of three Pd–Cu clusters used in the acidic HER, and $PdHCu_{11}(SR)_6(C{\equiv}CPh)_4$ only exhibited an overpotential of 50 mV at a current density of 10 mA cm^{-2}. Importantly,

Published on 09 2024. Downloaded on 28-05-26 15.06.19.

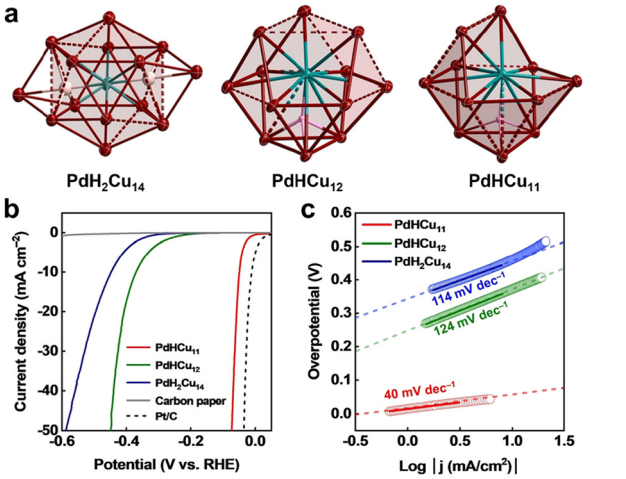

Fig. 4 (a) The core structures of $PdH_2Cu_{14}(SR)_6(C{\equiv}CPh)_6$, $PdHCu_{12}(SR)_6(C{\equiv}CPh)_4$, and $PdHCu_{11}(SR)_6(C{\equiv}CPh)_4$; ligands are omitted. Color codes: red = Cu, cyan = Pd, pink/white = H. (b) LSV curves for the three catalysts with carbon paper and Pt/C as comparison. (c) Corresponding Tafel plots of the three cluster catalysts. All measurements were conducted in Ar-saturated 0.5 M H_2SO_4 solution at 1 mV s^{-1}. Reproduced with permission from ref. 56. Copyright 2023 Wiley-VCH.

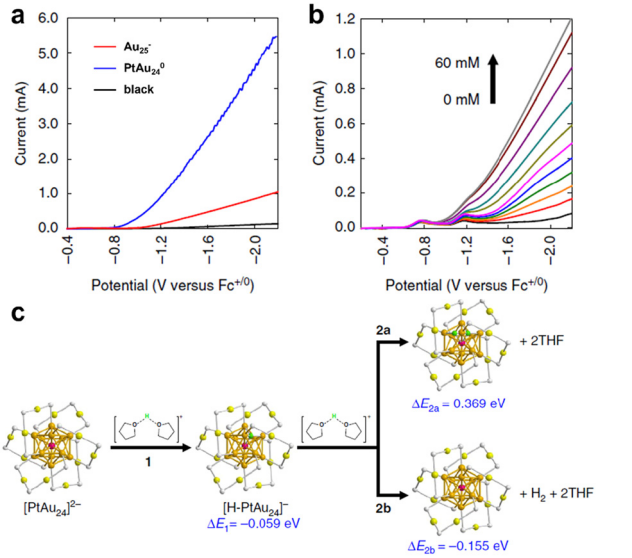

Fig. 5 (a) LSV curves of THF containing 0.1 M Bu_4NPF_6 and 1.0 M TFA solution for $Au_{25}(SR)_{18}^-$ and $PtAu_{24}(SR)_{18}^0$ clusters. (b) The polarization curves of 1 mM $PtAu_{24}(SR)_{18}^0$ in THF with different TFA concentrations. (c) The calculated energy of H_2 evolution on $PtAu_{24}(SR)_{18}^0$. Reproduced with permission from ref. 58. Copyright 2023 Nature Publishing Group.

$PdHCu_{11}(SR)_6(C{\equiv}CPh)_4$ exhibited almost constant HER activity and maintained the structural integrity. Fig. 4c shows the resulting Tafel slope plots, and significantly different Tafel slopes indicated that the reaction pathways are different at the surface of the three cluster catalysts. The rate-determining step for both $PdH_2Cu_{14}(SR)_6(C{\equiv}CPh)_6$ and $PdHCu_{12}(SR)_6(C{\equiv}CPh)_4$ systems was the Volmer pathway, while the rate-limiting step for $PdHCu_{11}(SR)_6(C{\equiv}CPh)_4$ was the Heyrovsky reaction, which implied that the open framework exposed Pd site was conducive to the adsorption of H and the promotion of the HER. The group later more strongly demonstrated the conclusion with the Pt-doped Cu–H cluster and that the $PtHCu_{11}(SR)_6(C{\equiv}CPh)_4$ cluster had the most outstanding performance among all HER cluster catalysts reported to date.[57]

The clusters can be applied not only for H_2 production in aqueous systems, but also in a wide range of organic systems. Kwak *et al.* catalysed electrochemical H_2 evolution in the tetrahydrofuran (THF) system using a centrally doped $PtAu_{24}(SR)_{18}^0$ cluster as a homogeneous catalyst in a system also containing 0.1 M tetra-*tert*-butylammonium hexafluoro-phosphonate (Bu_4NPF_6) and 1.0 M trifluoroacetic acid (TFA).[58] As can be seen from Fig. 5a, $Au_{25}(SR)_{18}^-$ exhibited a significant reduction current compared to the blank glassy carbon electrode, and the reduction current of the bimetallic cluster $PtAu_{24}(SR)_{18}^0$ was remarkably enhanced over the parent cluster, indicating that Pt doping can dramatically change the reduction potential of $PtAu_{24}(SR)_{18}^0$. Fig. 5b shows the polarization curve of 1 mM $PtAu_{24}(SR)_{18}^0$ cluster in THF solution with the change of TFA concentration. The two weak reduction peaks corresponded to the reduction potentials of $PtAu_{24}(SR)_{18}^{0/1-}$ and $PtAu_{24}(SR)_{18}^{1-/2-}$. When $PtAu_{24}(SR)_{18}^{2-}$ was produced, there was a pronounced H_2-producing current, which indicated that $PtAu_{24}(SR)_{18}^0$ displayed molecular-like properties to transfer individual electrons. Fig. 5c shows the H adsorption configuration and calculated energy in the THF system simulated by theoretical calculation. The protons involved in the HER process were simulated using protons dissolved by two THF molecules, and H was subsequently adsorbed on the surface of the cluster, a step that is thermodynamically advantageous. Step 2a in Fig. 5c is the Tafel pathway, which is endothermic. But process 2b is the Heyrovsky pathway, which is thermodynamically feasible. In addition, it was found that H atoms could spontaneously penetrate through the Au shell layer and adsorb onto the surface of Pt, so Pt was identified as the active site of the HER.

With the rapid development of scientific research, density functional theory (DFT) calculations have become an important characterization method to obtain the reaction intermediate states and adsorption energies through configuration optimization and simulation. Studies have also been reported on the adsorption of H atoms on clusters by first-principles DFT calculations.[59] In 2017, Jiang's group investigated the interaction of H with $Au_{25}(SR)_{18}$ and monoatom-doped $MAu_{24}(SR)_{18}$ (M = Pt, Pd, Ag, Cu, Hg or Cd) clusters by theoretical calculations.[60] It was found that the H atom exhibited metallic properties and can contribute 1s electrons to the superatomic free electron number. And when H was adsorbed on the cluster to form an 8e superatom, the binding energy was much stronger.

Subsequently, Hu and the co-workers modelled $Au_{22}(L^8)_6$ cluster protected by 1,8-bis(diphenylphosphine)octane (L^8) as a ligand, and demonstrated by DFT calculations that this

This journal is © The Royal Society of Chemistry 2024

Published on 09 2024. Downloaded on 28-05-26 15.06.19.

cluster was a promising catalyst for HER.[61] The $Au_{22}(L^8)_6$ cluster had eight coordinated unsaturated Au atoms at the waist of the cluster, which can serve as active sites for H adsorption. Calculations revealed that up to six of H atoms can be adsorbed onto the $Au_{22}(L^8)_6$ cluster, and the optimized H atom adsorption configuration is shown in Fig. 6a. The first four H atoms adsorbed were at the bridge sites of every two ligand-unsaturated Au, the fifth and sixth H atoms bridged on the top and bottom Au, and the latter Au was not coordination unsaturated. Fig. 6b shows the calculated adsorption energy (ΔE_H) and adsorption free energy (ΔG_H) for each H atom adsorbed on the cluster. It can be seen that the ΔG_H of the first six H atoms was close to 0 eV and that the second H was the strongest adsorbed. The seventh H atom can hardly adsorb on the cluster. Fig. 6c shows the Bader charge analysis of the $Au_{22}H_2(L^8)_6$ cluster with two H atoms adsorbed, and it can be seen that H atoms exhibited hydride-like properties with all negative charge. On the other hand, the Au attached to H showed an obvious lack of electrons. This suggested that the H adsorbed onto the phosphine ligand-capped Au cluster was characterized as a hydride, which differed from the metallic H in the thiol ligand-protected Au clusters.

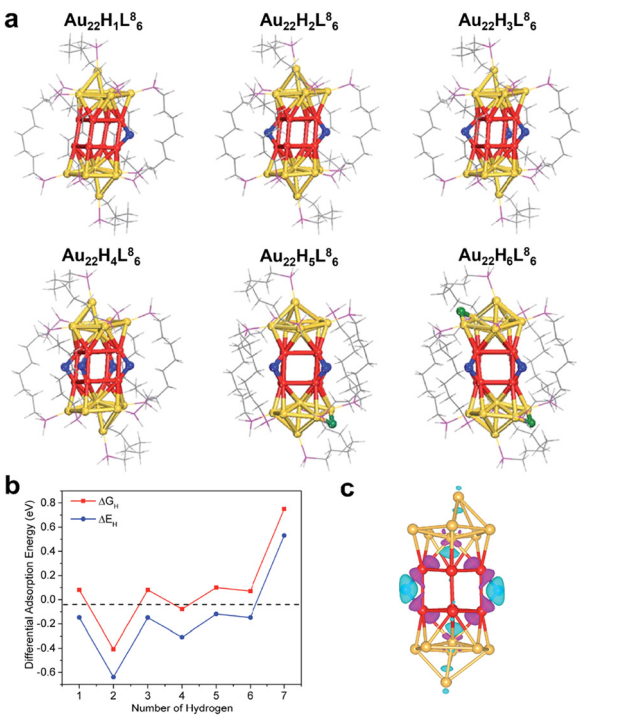

Fig. 6 (a) Optimized configurations of different amounts of H atoms adsorbed on $Au_{22}(L^8)_6$. (b) Calculated adsorption energies (ΔE_H) and adsorption free energies (ΔG_H). (c) The Bader charge of the $Au_{22}H_2(L^8)_6$ cluster with two H atoms adsorbed onto the $Au_{22}(L^8)_6$. Color codes: red/yellow = Au, blue/green/light grey = H, magenta = P, grey = C. Reproduced with permission from ref. 61. Copyright 2018 Royal Society of Chemistry.

3 Photocatalytic H_2 production

Photocatalytic H_2 production can be viewed as the process of catalysing water splitting to produce chemical energy H_2 using renewable solar energy assisted by a photocatalyst.[64,65] A favourable photocatalyst needs to satisfy the following conditions: a suitable band gap width and band position and effective ability to separate and transport electron–hole pairs.[66–68] Atomically precise metal clusters feature diverse energy levels, HOMO–LUMO (highest occupied molecular orbital–lowest unoccupied molecular orbital) transitions and special photo-absorption properties,[69,70] which make the clusters excellent for applications in photocatalysis. In recent years, chemists have achieved substantial progress in preparing composite photocatalysts by combining precise metal clusters with conventional semiconductors.[71,72] Orlov's group used sub-nm Au particle modification on CdS as a photocatalyst, which displayed amazing photocatalytic H_2 production performance.[73] However, the sub-nm particle had no resolved crystal structure, and was identified as bare Au_9 and Au_{11} by matrix-assisted laser desorption ionization-time of flight (MALDI-TOF) mass spectrometry and DFT simulations, which was the first ever demonstration of the potential of sub-nm Au particles for photocatalytic H_2 production.

As early as 2013, Jin's group demonstrated the high activity of Ni-based clusters as photocatalytic water reduction catalysts by using an Ir complex as a photosensitizer, triethylamine (TEA) as a sacrificial agent, and $Ni_6(SR)_{12}$ clusters as a water reducing catalyst, and the turnover numbers (TONs) and turnover frequencies (TOFs) can reach 3750 and 970 h^{-1}, respectively.[74] Ni^{II} first undergoes one electron reduction and protonation, possibly forming a hydride intermediate, followed by reduction of another proton to produce H_2. This study confirmed the promising potential of Ni-based clusters as catalysts for photocatalytic H_2 production from water reduction, which opened up a new mindset for designing photocatalysts.

Chen's group loaded benzyl thiol-protected $Ni_6(SR)_{12}$ cluster onto TiO_2.[75] This composite catalyst could significantly enhance the photocatalytic H_2 production activity under simulated sunlight using methanol as a sacrificial agent, and the molecular structure of the clusters remained unchanged during the catalytic process. $Ni_6(SR)_{12}$ (hereafter Ni_6) presented obvious characteristic absorption peaks in the UV-visible region. When Ni_6 cluster was loaded onto TiO_2, its solid-state UV spectrum exhibited a corresponding photoresponse, which was enhanced with the increase of Ni_6 cluster content. Fig. 7a shows the photocatalytic H_2 production performance of the catalysts with different Ni_6 cluster loadings, and increasing the cluster loading can enhance the photocatalytic H_2 generation production activity. The H_2 evolution activity of the catalyst only decreased slightly during the 10-cycle stability experiments. Fig. 7b shows the photocurrent density of Ni_6/TiO_2 and TiO_2, which was twice as high as that of pristine TiO_2 without the modification of Ni_6, implying that Ni_6 can improve the separation efficiency of photogenerated electron–hole pairs of TiO_2 and reduce the recombination rate. The electron density

Published on 09 2024. Downloaded on 28-05-26 15.06.19.

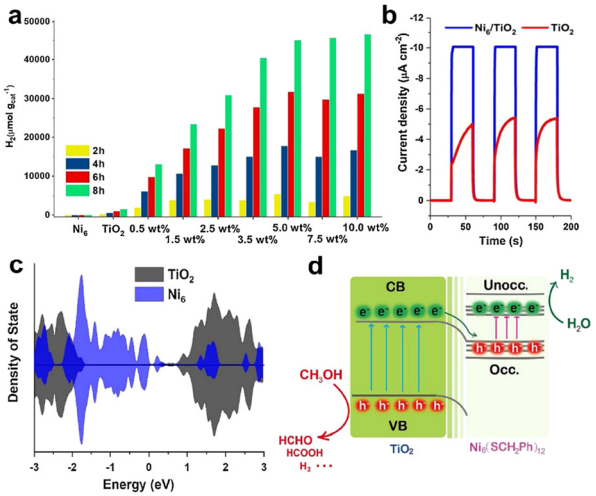

Fig. 7 (a) Photocatalytic H_2 production performance of catalysts with different cluster loadings in a mixture of distilled water and methanol (v/v = 80 mL/20 mL) with simulated solar light irradiation powered by a 300 W Xe lamp. (b) Photo-response currents of Ni_6/TiO_2 and TiO_2. (c) Electron density states of pristine TiO_2 and Ni_6 cluster. (d) Schematic diagram of the mechanism of photogenerated electron–hole pair transfer between TiO_2 and Ni_6 clusters. Reproduced with permission from ref. 75. Copyright 2021 Elsevier.

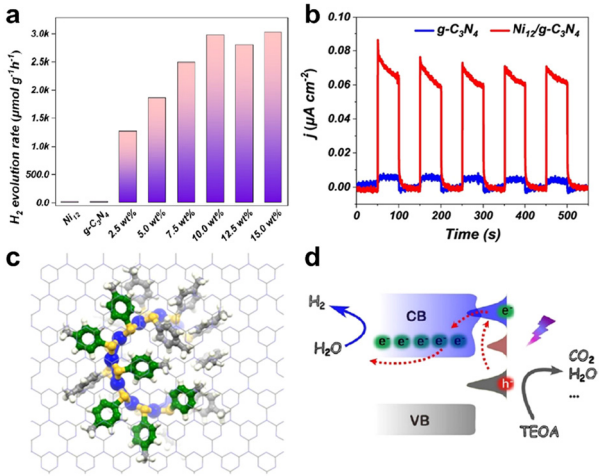

Fig. 8 (a) Photocatalytic H_2 production efficiency of catalysts with different Ni_{12} cluster loadings in a mixture of distilled water and methanol (v/v = 80 mL/20 mL) with simulated solar light irradiation powered by a 300 W Xe lamp. (b) Photo-response currents of $Ni_{12}/g\text{-}C_3N_4$ and $g\text{-}C_3N_4$. (c) *Ab initio* molecular dynamic snapshots of Ni_{12} loaded onto $g\text{-}C_3N_4$ systems at 10 ps. Color codes: blue = Ni, yellow = S, grey = C, white = H. (d) Schematic diagram of the mechanism of photogenerated electron–hole pair transfer between $g\text{-}C_3N_4$ and Ni_{12} clusters. Reproduced with permission from ref. 76. Copyright 2023 American Chemical Society.

state indicates that there was an overlap between the electron occupied orbital of Ni_6 and the conduction band of TiO_2, allowing the photogenerated electrons transfer from the TiO_2 conduction band to the occupied orbital of the excited Ni_6 cluster (Fig. 7c). Fig. 7d shows a schematic diagram of the mechanism of Ni_6 cluster enhancing the photocatalytic performance of TiO_2, showing the transfer path of photogenerated electron–hole pairs. It is worth mentioning that the non-bonding weak interaction between the ligands of the clusters and TiO_2 played a crucial role in this reaction.

Subsequently, they investigated the effect of cluster ligands on the photocatalytic performance using graphitic carbon nitride ($g\text{-}C_3N_4$) with delocalized π bonds as the carrier and $Ni_{12}(SR)_{24}$ (hereafter Ni_{12}) as the cocatalyst.[76] The Ni_{12} cluster possesses a ring structure, similar to that of a crown, and protected by 4-methylbenzenethiolates as a ligand. The absorption of the cluster in the UV-visible region mainly originated from the electron transition within the Ni–S ring structure of the cluster and the transition from the core structure to the π-bond of the benzene ring in the ligand. When exposed to ultraviolet radiation, electrons are transferred from the ring structure nucleus to the benzene ring ligand. Fig. 8a shows the H_2 generation efficiency of the catalysts with different cluster loadings under simulated sunlight radiation. While Ni_{12} and $g\text{-}C_3N_4$ alone were not photocatalytically active, Ni_{12}-modified $g\text{-}C_3N_4$ possessed an extremely high H_2 evolution rate, and the catalytic efficiency increased with the increase of cluster loading. Because the clusters featured significant absorption in the visible region, the photocurrent density of the composite catalyst was apparently amplified compared to fresh $g\text{-}C_3N_4$ (Fig. 8b). The activity of the catalyst was reduced by only 30% in a cycle stability test of greater than 24 hours. The interaction between the Ni_{12} cluster and $g\text{-}C_3N_4$ was simulated by molecular dynamics, and it was found that the benzene ring on the cluster ligand was parallel to the $g\text{-}C_3N_4$ plane, resulting in π–π conjugated interaction, which connected the charge transfer between the cluster and the carrier, and facilitated the effective separation of photogenerated electrons and holes of the composite catalyst to enhance the catalytic activity (benzene rings are shown in green in Fig. 8c). The mechanism of the conjugation interaction to improve the photocatalytic H_2 evolution performance is shown in Fig. 8d and marked by red arrows. Under light irradiation, the ground state electrons of Ni_{12} were excited to produce photogenerated electron–hole pairs. The photogenerated electrons jump to the conduction band of $g\text{-}C_3N_4$ due to the π–π interactions, and are then captured by the surface to produce H_2. This study visualized the weak cluster–support interaction in the composite photocatalysts as the π–π conjugated interaction.

In addition to Ni-based clusters, Cu-based clusters have also been shown to be outstanding catalysts for photochemical H_2 production. The Cu cluster family has developed gradually, which has more enriched crystallographic structure compared to Ni clusters. Gao's group reported a precise $Cu_{20}O_1(C_{20}H_{24}O_2)_{12}(CH_3COO)_6$ cluster (hereafter UNJ-Cu_{20}) protected by ethinylestradiol ($C_{20}H_{24}O_2$) ligands and acetic acid (CH_3COOH) molecules.[77] Unlike previously reported Cu clusters, the additional hydroxyl group on $C_{20}H_{24}O_2$ can modulate the hydrophilicity of UNJ-Cu_{20}. Combining UNJ-Cu_{20} and TiO_2 nanosheets (NSs) can form a highly efficient composite

 This journal is © The Royal Society of Chemistry 2024

Published on 09 2024. Downloaded on 28-05-26 15.06.19.

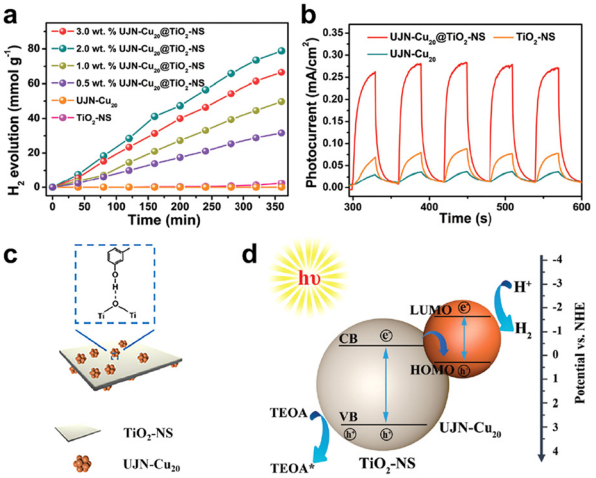

Fig. 9 (a) Photocatalytic H_2 production rates of composite catalysts with different UNJ-Cu_{20} cluster loadings using a 300 W xenon lamp as the light source to simulate sunlight. (b) Photo-response currents density of UNJ-Cu_{20}, TiO_2-NS and UNJ-Cu_{20}/TiO_2-NS. (c) Schematic diagram of the interaction of UNJ-Cu_{20} with TiO_2-NS surface. (d) Schematic illustration of the relative positions of the UNJ-Cu_{20} and TiO_2-NS energy bands and the electron transfer mechanism over the composite catalysts. Reproduced with permission from ref. 77. Copyright 2021 Royal Society of Chemistry.

H_2 evolution photocatalyst. As shown in Fig. 9a, the photocatalytic H_2 generation performance of UJN-Cu_{20}@TiO_2-NS composites with different loadings of UJN-Cu_{20} was demonstrated by using a 300 W xenon lamp to simulate sunlight. The original TiO_2-NS or UJN-Cu_{20} could only produce trace amounts of H_2. The H_2 production activity of UJN-Cu_{20}@TiO_2-NS nanocomposites was significantly enhanced, with an optimal H_2 production rate of 13 mmol g^{-1} h^{-1} at 2% UJN-Cu_{20} loading. Moreover, UJN-Cu_{20}@TiO_2-NS nanocomposite maintained high H_2 production activity after 5 cycles. Fig. 9b shows the photocurrent response curve to investigate the photoconversion ability of the catalyst. Both TiO_2-NS and UJN-Cu_{20} exhibited weak photocurrent responses. And the composite catalyst possesses a significantly enhanced photoelectric response, indicating that the synergistic effect of the UJN-Cu_{20} cluster and TiO_2-NS could promote the separation of photoelectrons and holes. As for the interaction between UJN-Cu_{20} clusters and TiO_2-NS, UJN-Cu_{20} was bound to the surface of TiO_2-NS by hydrogen bonding *via* the hydroxyl group on the ligand (Fig. 9c). Fig. 9d illustrates the relative positions of energy bands of UJN-Cu_{20} and TiO_2-NS as well as the electron transfer mechanism on the composite catalyst. The electrons were excited, when the light energy was larger than the band gap of both. The electrons from the TiO_2-NS conduction band combined with the holes in the HOMO level of UJN-Cu_{20}, retaining the electrons from the LUMO level of UJN-Cu_{20}. Triethanolamine (TEOA) could capture the holes with strong oxidation capacity in the TiO_2-NS valence band. By constructing a Z-type photocatalytic system, the separation of photoelectrons and holes was significantly promoted.

Loading Cu-based clusters onto semiconductor TiO_2 can lead to efficient photocatalysts; on the other hand, self-assembled cluster-based metal organic frameworks (MOFs), a porous network structure with periodicity by connecting cluster nodes with organic ligands, also improved the stability of the clusters. Moreover, the MOFs also could maximize the accessibility of the unsaturated active sites in the spatial separation structure. Xu *et al.* synthesized a $Cu_8(SN)_4(^tBuS)_4$ (SN = 4-(4-pyridinyl)thiazole-2-thiol) cluster with the precise structure shown in Fig. 10a.[78] And the Cu-MOF was obtained by using $Cu_8(SN)_4(^tBuS)_4$ as a metal cluster node, and SN with a double coordination structure as an ideal grafting ligand, with Cu cluster attached at one end and uncoordinated pyridine nitrogen atoms linked to Cu at the other end during the self-assembly process. Fig. 10a shows the mechanism of construction of the Cu cluster-based MOF. When fluorescein (FL) and triethylamine (TEA) were used as photosensitizers and sacrificial agents, the ordered-structured Cu-MOF exhibited excellent photocatalytic H_2 production activity (Fig. 10b), and the Cu-MOF displayed the recycling of heterogeneous catalysts. The photo-responsive current densities of $Cu_8(SN)_4(^tBuS)_4$ and Cu-MOF were compared in Fig. 10c, and the introduction of the FL significantly enhanced the photocurrent of Cu-MOF, which indicated that a large number of photogenerated electrons were transferred from the photosensitizer to the Cu-MOF catalyst as well as the efficient separation and transfer of photogenerated electrons. Compared with $Cu_8(SN)_4(^tBuS)_4$ units, the ordered porous frame structure enabled Cu-MOF to carry out charge transfer efficiently, which was the main reason for its enhanced photocatalytic performance. Furthermore, Jiang and his colleagues reported that $MAg_{24}(SR)_{18}$ (M = Ag, Pd, Pt, and Au) encapsulated in MOFs exhibited outstanding photocatalytic H_2 production activity, which was attributed to the

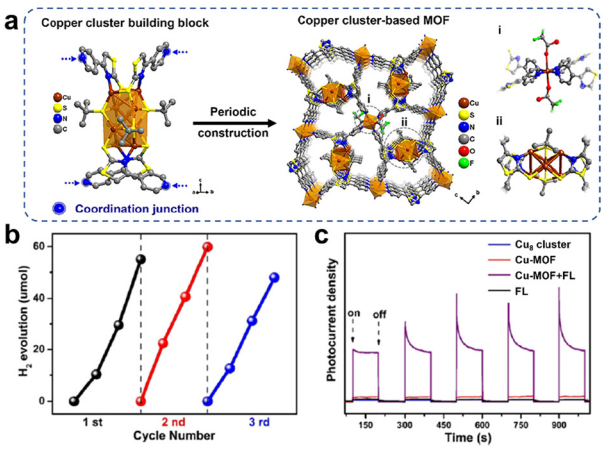

Fig. 10 (a) Schematic diagram of the synthesis of $Cu_8(SN)_4(^tBuS)_4$ cluster-based MOFs (Cu-MOF) through self-assembly of copper cluster units. (b) Recyclability of Cu-MOF for photocatalytic H_2 production in a mixed solution of ethanol and water (v/v = 1/1) with FL and TEA as the photosensitizer and sacrificial agent. (c) Photo-response currents density of $Cu_8(SN)_4(^tBuS)_4$ and Cu-MOF. Reproduced with permission from ref. 78. Copyright 2023 Royal Society of Chemistry.

Published on 09 2024. Downloaded on 28-05-26 15.06.19.

fact that the metal clusters generated a charge transfer pathway similar to that of a Z-type heterojunction under visible irradiation, which facilitated charge separation.[79]

In addition to monometallic Cu clusters, Mo–Cu bimetallic clusters have also been reported for photocatalytic H_2 production. Zang's group introduced $MoOS_3^{2-}$ unit into Cu cluster and prepared a series of atomically precise $Cu_6(MoOS_3)_2(C_7H_7S)_2(PPh_3)_4{\cdot}xCH_3CN$ (Cu_6Mo_2, C_7H_7S = benzyl mercaptan).[80] The introduction of $MoOS_3^{2-}$ could improve the structural stability of Cu clusters and introduce new active sites. The composite catalyst loaded with Fe_3O_4 exhibited excellent catalytic activity and stability in the photocatalytic H_2 production reaction due to the electronic effects of ligands that can modify the HOMO–LUMO of the cluster. The electrons on the LUMO of FL are trapped by holes on the HOMO of Cu_6Mo_2 under light radiation. As a result, the electrons are highly reductive on the LUMO of Cu_6Mo_2 and thus participate in the generation of H_2. This kind of new copper clusters bring new vitality to photocatalytic hydrogen production catalysts.

It is well known that gold bulk is chemically inert. Recently, Xiao's group constructed an interfacial charge-controlled Z-type heterojunction photocatalyst based on $Au_{25}(GS)_{18}$ (GSH = glutathione) cluster.[81] Fig. 11a shows a schematic diagram of the preparation of $MoSe_2/CdSe/Au_{25}$ (M/C/A) heterojunction catalyst. First, $MoSe_2$ nanosheets were modified with a layer of mercaptoacetic acid (MAA) to make the surface negatively charged. The surface of CdSe quantum dots was positively charged by surface modified 2-aminoethanethiol (AET). The charge-modified $MoSe_2$ nanosheets and CdSe quantum dots were self-assembled to form the binary heterostructure as shown in Fig. 11b, and the surface of the composite structure was positively charged. GSH-protected Au_{25} cluster was assembled with a binary heterostructure to form a ternary heterostructure, as shown in Fig. 11c. Fig. 11d shows the photocatalytic H_2 production activities of each component.

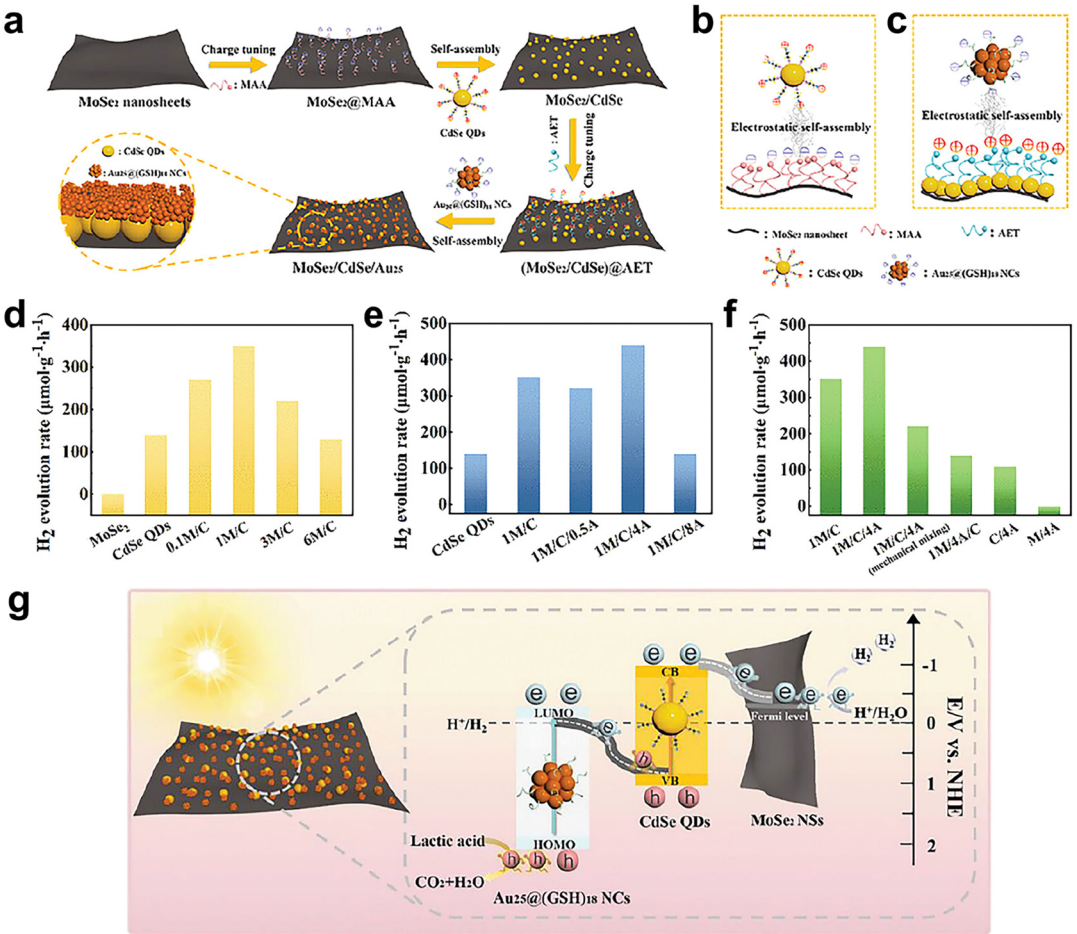

Fig. 11 (a) Schematic diagram of the preparation of $MoSe_2/CdSe/Au_{25}$ (M/C/A) heterojunction catalyst. (b) $MoSe_2/CdSe$ heterostructure. (c) $MoSe_2/CdSe/Au_{25}$ ternary heterostructure. (d) Photocatalytic H_2 production activities of $MoSe_2$, CdSe and M_x/C (x = 0.1, 1, 3 and 6). (e) Photocatalytic H_2 production activities of CdSe, 1M/C and $1M/C/A_x$ (x = 0.5, 4, and 8). (f) Photocatalytic H_2 production activities of 1M/C, 1M/C/4A produced by surface charge regulation and simple physical mixing under visible light irradiation (λ > 420 nm) in Na_2SO_4 aqueous solution (pH = 6.69). (g) Scheme of the electron transfer mechanism of catalyst. Reproduced with permission from ref. 81. Copyright 2023 Wiley-VCH.

This journal is © The Royal Society of Chemistry 2024

Published on 09 2024. Downloaded on 28-05-26 15.06.19.

The $MoSe_2$ nanosheets alone were almost inactive, CdSe quantum dots were poorly active, and the catalytic activity of $MoSe_2$/CdSe (M/C) was significantly improved. Fig. 11e compares the effect of the introduction of $Au_{25}(GSH)_{18}$ on the catalytic performance of $MoSe_2$/CdSe binary heterostructures. The highest catalytic activity was obtained when the content of $Au_{25}(GSH)_{18}$ was 4 mL (1M/C/4A), which highlighted the great importance of $Au_{25}(GSH)_{18}$ in the catalysis of ternary heterostructures. Fig. 11f compares the photocatalytic activity of the composite catalyst produced by simple physical mixing without surface charge regulation. The experimental results demonstrated that all of the three components along with charge regulation were indispensable for improving the H_2 production activity. The excellent catalytic activity was derived from the fact that $MoSe_2$ can accelerate the migration of photoelectrons from CdSe quantum dots to $MoSe_2$ nanosheets, and reduce the carrier recombination rate of CdSe quantum dots. In addition, the 1M/C/4A catalyst exhibited great cycling stability, with no decay in activity during four cycles of the reaction. Fig. 11g presents a schematic diagram of the electron transfer mechanism of the catalyst. Under visible light irradiation, the HOMO of $Au_{25}(GSH)_{18}$ produced photogenerated electrons onto the LUMO, and the CdSe quantum dots were also photoexcited to generate charge carriers. The electrons at the LUMO level of $Au_{25}(GSH)_{18}$ clusters rapidly combine with the holes in the valence band of CdSe quantum dots. At the same time, the electrons in the conduction band of CdSe quantum dots migrated to the neighboring $MoSe_2$ nanosheets to complete

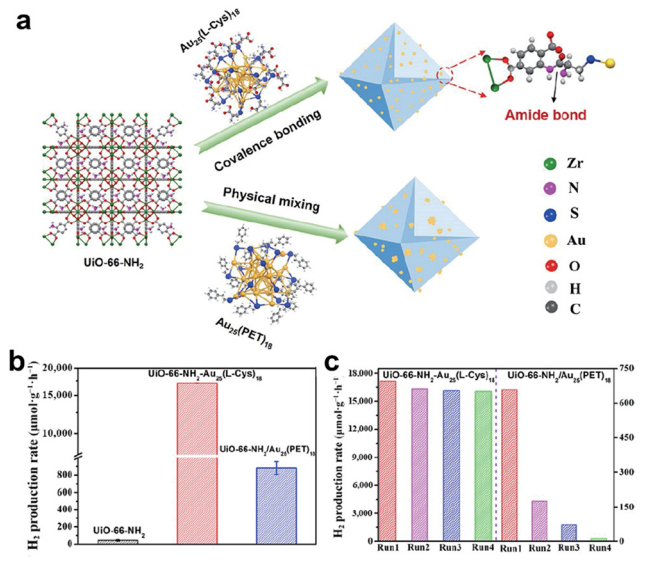

Fig. 12 (a) Schematic diagram of Au_{25}(L-Cys)$_{18}$ bound to UiO-66-NH_2 through covalent bridge strategy. (b) Comparison of the photocatalytic H_2 production performance of UiO-66-NH_2, covalent bonded UiO-66-NH_2-Au_{25}(L-Cys)$_{18}$ and physically mixed UiO-66-NH_2/Au_{25}(PET)$_{18}$ with ErB and TEOA as the photosensitizer and sacrificial agent. The light source was a 300 W xenon lamp with a >420 nm filter. (c) Comparison of cycling stability of UiO-66-NH_2-Au_{25}(L-Cys)$_{18}$ and UiO-66-NH_2/Au_{25}(PET)$_{18}$. Reproduced with permission from ref. 82. Copyright 2023 Springer Nature.

Table 2 Photocatalytic H_2 generation performance of precise metal cluster catalysts reported

Catalysts	Co-catalyst	Amount of catalyst (mg)	Light source	Sacrificial agent (vol%)	Activity	Ref.
$Ni_6(SR)_{12}/TiO_2$	$Ni_6(SR)_{12}$	20	300 W Xe lamp	Methanol (20)	5600 μmol g^{-1} h^{-1}	75
$Ni_{12}(SR)_{24}/C_3N_4$	$Ni_{12}(SR)_{24}$	10	50 W Xe lamp	Triethanolamine (20)	3000 μmol g^{-1} h^{-1}	76
Cu_{20}@TiO_2-NS	Cu_{20}	—	300 W Xe lamp (λ > 420 nm)	Triethanolamine (—)	13 mmol g^{-1} h^{-1}	77
Cu_6-MOF	Cu_6	2	300 W Xe lamp (λ > 420 nm)	Triethanolamine (5)	127.98 mmol per g per 9 h	78
$MoSe_2$/CdSe/$Au_{25}(SR)_{18}$	$Au_{25}(SR)_{18}$	10	300 W Xe lamp (λ > 420 nm)	Lactic acid (10)	140 μmol g^{-1} h^{-1}	81
UiO-66-NH_2-$Au_{25}(SR)_{18}$	$Au_{25}(SR)_{18}$	5	300 W Xe lamp (λ > 420 nm)	Triethanolamine (10)	17 012.045 μmol g^{-1} h^{-1}	82
$Au_{25}(SR)_{18}$/g-C_3N_4	$Au_{25}(SR)_{18}$	20	300 W Xe lamp (λ > 420 nm)	Triethanolamine (10)	320 μmol g^{-1} h^{-1}	83
$Au_{24}Pt(SR)_{18}$–$BaLa_4Ti_4O_{15}$	$Au_{24}Pt(SR)_{18}$	500	400 W high-pressure Hg lamp	Methanol (10)	5000 μmol h^{-1}	84
$Au_{25}(SR)_{18}$–$BaLa_4Ti_4O_{15}$	$Au_{25}(SR)_{18}$	500	400 W high-pressure Hg lamp	—	500 μmol h^{-1}	85
$Au_{101}(PPh_3)_{21}Cl_5$–AlSrTiO$_3$-r-GO	$Au_{101}(PPh_3)_{21}Cl_5$	7	UV LED (365 nm, 83 mW cm^{-2})	Methanol (33.3)	0.5 μmol g^{-1} h^{-1}	86
$Au_{25}(SR)_{18}$–Cr_2O_3–$BaLa_4Ti_4O_{15}$	$Au_{25}(SR)_{18}$	500	400 W high-pressure Hg lamp	Methanol (10)	4697 μmol h^{-1}	87

Published on 09 2024. Downloaded on 28-05-26 15.06.19.

the Z-scheme charge transfer. This work inspired the researchers to optimize the catalytic reaction performance by manipulating the surface charge catalyst.

In addition to interfacial charge regulation, Zhu *et al.* also proposed a covalent bridge strategy connecting atomically precise Au_{25}(L-Cys)$_{18}$ (L-Cys = L-cysteine) cluster with metal–organic frameworks to enhance the activity and stability of photocatalytic H_2 production.[82] Fig. 12a shows a schematic diagram of –COOH on the Au_{25}(L-Cys)$_{18}$ ligand bound to –NH_2 on UiO-66-NH_2 by a dehydration condensation reaction with an amide covalent bond. Through a covalent bridge strategy, the Au_{25}(L-Cys)$_{18}$ cluster was uniformly and densely embedded throughout UiO-66-NH_2. A physical mixture of Au_{25}(PET)$_{18}$ and UiO-66-NH_2 was also prepared for comparison. Fig. 12b compares the photocatalytic H_2 production performance of UiO-66-NH_2, covalent bonded UiO-66-NH_2-Au_{25}(L-Cys)$_{18}$ and physically mixed UiO-66-NH_2/Au_{25}(PET)$_{18}$. UiO-66-NH_2-Au_{25}(L-Cys)$_{18}$ exhibited the optimal photocatalytic H_2 production rate, which was 90 times higher than that of the original UiO-66-NH_2. Moreover, the UiO-66-NH_2-Au_{25}(L-Cys)$_{18}$ catalyst linked *via* covalent bonding displayed outstanding stability (Fig. 12c). The UiO-66-NH_2/Au_{25}(PET)$_{18}$ catalyst by simple mixing in the second cycle showed a significant decrease in catalytic activity. This is attributed to the metal–support interaction created by the covalent bond between UiO-66-NH_2 and Au_{25}(L-Cys)$_{18}$, which can facilitate charge transport and inhibit charge–hole recombination. We also list a comprehensive range of studies of precise metal clusters as photocatalysts in Table 2, including test conditions and catalytic activities, without going into detail.

4 Conclusions

In summary, we have concentrated on summarizing the development of atomically precise metal clusters in electrochemical and photocatalytic hydrogen production in the last few years. Due to the resolvable crystallographic structure of metal clusters, they provide a promising research platform for understanding the relationship between catalytic performance and structure. Many achievements have been witnessed in the application of precise clusters for electrocatalytic and photocatalytic H_2 production. With the further development of scientific research, the researchers are more in pursuit of superior catalytic performance, and how to enhance the efficiency of electrocatalysis and photocatalysis remains a challenge for current research. For electrochemical H_2 evolution catalysts, understanding the electron transfers between the catalyst and electrode surface as well as the catalyst and reaction substrate is crucial for designing high-performance electrocatalysts. For photocatalytic H_2 production, how to effectively promote the separation of photogenerated electron–hole pairs and inhibit their recombination is the key to enhancing the photocatalytic efficiency. Metal clusters with extraordinary optical absorption urgently need to be designed to have the ability to capture light from the visible to the infrared and act as photosensitizers in photocatalytic systems. In addition, ligand-protected metal clusters are fragile in both electrocatalytic and photocatalytic systems, and improving the structural stability of the clusters is conducive to promote catalytic stability. The monitoring of active sites reported so far is usually realized by DFT calculations. Therefore, *in situ* characterization techniques are of great interest for experimentally detecting active sites and tracking cluster structure evolution. It is expected that the development of atomically precise metal clusters in the field of electrochemical and photocatalytic H_2 production will fill the gap between single-atom catalysis and nanoparticle catalysis and bring new opportunities for understanding the catalytic mechanism.

Data availability

This is a review, in which the data supporting this article have been reported.

Conflicts of interest

There are no conflicts to declare.

Acknowledgements

We acknowledge the financial support from the National Natural Science Foundation of China (22125202, 21932004 and 22302091) and the Natural Science Foundation of Jiangsu Province (BK20220033).

References

1 S. Shiva Kumar and V. Himabindu, *Mater. Sci. Energy Technol.*, 2019, **2**, 442–454.
2 K. Perović, S. Morović, A. Jukić and K. Košutić, *Materials*, 2023, **16**, 6319.
3 E. Fernandez, L. Santamaria, M. Artetxe, M. Amutio, A. Arregi, G. Lopez, J. Bilbao and M. Olazar, *Fuel*, 2022, **312**, 122910.
4 V. Palma, F. Castaldo, P. Ciambelli and G. Iaquaniello, *Appl. Catal., B*, 2014, **145**, 73–84.
5 J. Wang, J. Liu, L. Zhang, S. Dai, A. Li and J. Chen, *Fuel*, 2022, **327**, 125076.
6 L. Feng, M. Dong, B. Qin, J. Pang and S. Babaee, *Energy*, 2024, **291**, 130379.
7 H. L. Huynh, W. M. Tucho, X. Yu and Z. Yu, *J. Cleaner Prod.*, 2020, **264**, 121720.
8 X. Hong, V. B. Thaore, S. S. Garud, I. A. Karimi, S. Farooq, X. Wang, A. K. Usadi and B. R. Chapman, *Int. J. Hydrogen Energy*, 2023, **48**, 8743–8755.
9 J. Wu, Y. Tao, C. Zhang, Q. Zhu, D. Zhang and G. Li, *J. Hazard. Mater.*, 2023, **443**, 130363.

 This journal is © The Royal Society of Chemistry 2024

Published on 09 2024. Downloaded on 28-05-26 15.06.19.

10 M. Zhang, J. Guan, Y. Tu, S. Chen, Y. Wang, S. Wang, L. Yu, C. Ma, D. Deng and X. Bao, *Energy Environ. Sci.*, 2020, **13**, 119–126.
11 R. Zhang, Y. Li, X. Zhou, A. Yu, Q. Huang, T. Xu, L. Zhu, P. Peng, S. Song, L. Echegoyen and F. F. Li, *Nat. Commun.*, 2023, **14**, 2460.
12 J. Zhu, L. Hu, P. Zhao, L. Y. S. Lee and K. Y. Wong, *Chem. Rev.*, 2020, **120**, 851–918.
13 X. W. Lv, W. W. Tian and Z. Y. Yuan, *Electrochem. Energy Rev.*, 2023, **6**, 23.
14 Q. Liu, C. Zeng, Z. Xie, L. Ai, Y. Liu, Q. Zhou, J. Jiang, H. Sun and S. Wang, *Appl. Catal., B*, 2019, **254**, 443–451.
15 J. Wu, H. Zhong, Z. F. Huang, J. J. Zou, X. Zhang, Y. C. Zhang and L. Pan, *Nanoscale*, 2024, **16**, 9169–9185.
16 Z. Kang, M. A. Khan, Y. Gong, R. Javed, Y. Xu, D. Ye, H. Zhao and J. Zhang, *J. Mater. Chem. A*, 2021, **9**, 6089–6108.
17 G. Zhao, Y. Jiang, S. X. Dou, W. Sun and H. Pan, *Sci. Bull.*, 2021, **66**, 85–96.
18 J. Ding, H. Yang, S. Zhang, Q. Liu, H. Cao, J. Luo and X. Liu, *Small*, 2022, **18**, 2204524.
19 B. J. Ng, L. K. Putri, X. Y. Kong, Y. W. Teh, P. Pasbakhsh and S. P. Chai, *Adv. Sci.*, 2020, **7**, 1903171.
20 M. U. Shahid, T. Najam, M. H. Helal, I. Hossain, S. M. El-Bahy, Z. M. El-Bahy, A. ur Rehman, S. S. A. Shah and M. A. Nazir, *Int. J. Hydrogen Energy*, 2024, **62**, 1113–1138.
21 H. Nazir, C. Louis, S. Jose, J. Prakash, N. Muthuswamy, M. E. M. Buan, C. Flox, S. Chavan, X. Shi, P. Kauranen, T. Kallio, G. Maia, K. Tammeveski, N. Lymperopoulos, E. Carcadea, E. Veziroglu, A. Iranzo and A. M. Kannan, *Int. J. Hydrogen Energy*, 2020, **45**, 13777–13788.
22 R. Jin, C. Zeng, M. Zhou and Y. Chen, *Chem. Rev.*, 2016, **116**, 10346–10413.
23 X. Zou, X. Kang and M. Zhu, *Chem. Soc. Rev.*, 2023, **52**, 5892–5967.
24 O. Lopez-Acevedo, K. A. Kacprzak, J. Akola and H. Häkkinen, *Nat. Chem.*, 2010, **2**, 329–334.
25 X. Liu, E. Wang, M. Zhou, Y. Wan, Y. Zhang, H. Liu, Y. Zhao, J. Li, Y. Gao and Y. Zhu, *Angew. Chem., Int. Ed.*, 2022, **61**, e202207685.
26 S. Li, A. V. Nagarajan, X. Du, Y. Li, Z. Liu, D. R. Kauffman, G. Mpourmpakis and R. Jin, *Angew. Chem., Int. Ed.*, 2022, **61**, e202211771.
27 H. Yan, H. Xiang, J. Liu, R. Cheng, Y. Ye, Y. Han and C. Yao, *Small*, 2022, **18**, 2200812.
28 Y. Sun, X. Cai, W. Hu, X. Liu and Y. Zhu, *Sci. China: Chem.*, 2021, **64**, 1065–1075.
29 X. Yuan and M. Zhu, *Inorg. Chem. Front.*, 2023, **10**, 3995–4007.
30 K. Kwak and D. Lee, *Acc. Chem. Res.*, 2019, **52**, 12–22.
31 Z. Song, T. Shen, Y. Hu, G. Liu, S. Bai, X. Sun, S. M. Xu and Y. F. Song, *Nanoscale*, 2023, **15**, 11867–11874.
32 M. Wu, F. Dong, Y. Yang, X. Cui, X. Liu, Y. Zhu, D. Li, S. Omanovic, S. Sun and G. Zhang, *Electrochem. Energy Rev.*, 2024, **7**, 10.
33 T. H. Chiu, J. H. Liao, R. P. B. Silalahi, M. N. Pillay and C. W. Liu, *Nanoscale Horiz.*, 2024, **9**, 675–692.
34 Z. Pu, I. S. Amiinu, R. Cheng, P. Wang, C. Zhang, S. Mu, W. Zhao, F. Su, G. Zhang, S. Liao and S. Sun, *Nano-Micro Lett.*, 2020, **12**, 21.
35 N. Dubouis and A. Grimaud, *Chem. Sci.*, 2019, **10**, 9165–9181.
36 P. Zhu, X. Xiong and D. Wang, *Nano Res.*, 2022, **15**, 5792–5815.
37 H. Chen, Y. Zhou, W. Guo and B. Y. Xia, *Chin. Chem. Lett.*, 2022, **33**, 1831–1840.
38 Y. Wang, H. Zhuo, X. Zhang, Y. Li, J. Yang, Y. Liu, X. Dai, M. Li, H. Zhao, M. Cui, H. Wang and J. Li, *J. Mater. Chem. A*, 2019, **7**, 24328–24336.
39 Z. Zhong, Y. Tu, L. Zhang, J. Ke, C. Zhong, W. Tan, L. Wang, J. Zhang, H. Song, L. Du and Z. Cui, *ACS Catal.*, 2024, **14**, 2917–2923.
40 W. Choi, G. Hu, K. Kwak, M. Kim, D.-e. Jiang, J. P. Choi and D. Lee, *ACS Appl. Mater. Interfaces*, 2018, **10**, 44645–44653.
41 A. M. Abudayyeh, M. S. Bennington, J. Hamonnet, A. T. Marshall and S. Brooker, *Dalton Trans.*, 2024, **53**, 6207–6214.
42 C. R. Ratwani, S. Karunarathne, A. R. Kamali and A. M. Abdelkader, *ACS Appl. Mater. Interfaces*, 2024, **16**, 5847–5856.
43 X. Gao and W. Chen, *Chem. Commun.*, 2017, **53**, 9733–9736.
44 K. M. Sithar Shahul, V. Packirisamy and P. Pandurangan, *Int. J. Hydrogen Energy*, 2024, **62**, 1067–1076.
45 S. Zhao, R. Jin, Y. Song, H. Zhang, S. D. House, J. C. Yang and R. Jin, *Small*, 2017, **13**, 1701519.
46 S. Gratious, A. Karmakar, D. Kumar, S. Kundu, S. Chakraborty and S. Mandal, *Nanoscale*, 2022, **14**, 7919–7926.
47 Y. Du, J. Xiang, K. Ni, Y. Yun, G. Sun, X. Yuan, H. Sheng, Y. Zhu and M. Zhu, *Inorg. Chem. Front.*, 2018, **5**, 2948–2954.
48 W. L. Mu, Y. T. Luo, P. K. Xia, Y. L. Jia, P. Wang, Y. Pei and C. Liu, *Inorg. Chem.*, 2024, **63**, 6767–6775.
49 H. Mousavi, Y. Yin, S. K. Sharma, C. T. Gibson, V. Golovko, G. G. Andersson, C. J. Shearer and G. F. Metha, *J. Phys. Chem. C*, 2021, **126**, 246–260.
50 L. Sahoo, A. Devi and A. Patra, *ACS Sustainable Chem. Eng.*, 2023, **11**, 4187–4196.
51 B. Kumar, T. Kawawaki, N. Shimizu, Y. Imai, D. Suzuki, S. Hossain, L. V. Nair and Y. Negishi, *Nanoscale*, 2020, **12**, 9969–9979.
52 Y. Li, S. Li, A. V. Nagarajan, Z. Liu, S. Nevins, Y. Song, G. Mpourmpakis and R. Jin, *J. Am. Chem. Soc.*, 2021, **143**, 11102–11108.
53 Y. Jo, M. Choi, M. Kim, J. S. Yoo, W. Choi and D. Lee, *Bull. Korean Chem. Soc.*, 2021, **42**, 1672–1677.
54 Y. Tang, F. Sun, X. Ma, L. Qin, G. Ma, Q. Tang and Z. Tang, *Dalton Trans.*, 2022, **51**, 7845–7850.
55 G. Ma, Y. Tang, L. Chen, L. Qin, Q. Shen, L. Wang and Z. Tang, *Eur. J. Inorg. Chem.*, 2022, e202200176.
56 R. P. Brocha Silalahi, Y. Jo, J. H. Liao, T. H. Chiu, E. Park, W. Choi, H. Liang, S. Kahlal, J. Y. Saillard, D. Lee and C. W. Liu, *Angew. Chem., Int. Ed.*, 2023, **62**, e202301272.
57 R. P. Brocha Silalahi, H. Liang, Y. Jo, J. H. Liao, T. H. Chiu, Y. Y. Wu, X. Wang, S. Kahlal, Q. Wang, W. Choi, D. Lee,

Published on 09 2024. Downloaded on 28-05-26 15.06.19.

J. Y. Saillard and C. W. Liu, *Chem. – Eur. J.*, 2024, **30**, e202303755.
58 K. Kwak, W. Choi, Q. Tang, M. Kim, Y. Lee, D.-e. Jiang and D. Lee, *Nat. Commun.*, 2017, **8**, 14723.
59 O. López-Estrada, N. Mammen, L. Laverdure, M. M. Melander, H. Häkkinen and K. Honkala, *ACS Catal.*, 2023, **13**, 8997–9006.
60 G. Hu, Q. Tang, D. Lee, Z. Wu and D.-e. Jiang, *Chem. Mater.*, 2017, **29**, 4840–4847.
61 G. Hu, Z. Wu and D.-e. Jiang, *J. Mater. Chem. A*, 2018, **6**, 7532–7537.
62 H. Shen, Q. Zhu, J. Xu, K. Ni, X. Wei, Y. Du, S. Gao, X. Kang and M. Zhu, *Nanoscale*, 2023, **15**, 14941–14948.
63 X. Liu, Y. Tang, L. Chen, L. Wang, Y. Liu and Z. Tang, *Int. J. Hydrogen Energy*, 2024, **53**, 300–307.
64 S. Tasleem, M. Tahir and W. A. Khalifa, *Int. J. Hydrogen Energy*, 2021, **46**, 14148–14189.
65 S. Xiong, R. Tang, D. Gong, Y. Deng, J. Zheng, L. Li, Z. Zhou, L. Yang and L. Su, *Chin. J. Catal.*, 2022, **43**, 1719–1748.
66 E. Nikoloudakis, I. López-Duarte, G. Charalambidis, K. Ladomenou, M. Ince and A. G. Coutsolelos, *Chem. Soc. Rev.*, 2022, **51**, 6965–7045.
67 J. Wen, J. Xie, Z. Yang, R. Shen, H. Li, X. Luo, X. Chen and X. Li, *ACS Sustainable Chem. Eng.*, 2017, **5**, 2224–2236.
68 Y. Yang, C. Zhou, W. Wang, W. Xiong, G. Zeng, D. Huang, C. Zhang, B. Song, W. Xue, X. Li, Z. Wang, D. He, H. Luo and Z. Ouyang, *Chem. Eng. J.*, 2021, **405**, 126547.
69 Y. Zhao, Z. Niu, J. Zhao, L. Xue, X. Fu and J. Long, *Electrochem. Energy Rev.*, 2023, **6**, 14.
70 G. Li, H. Abroshan, C. Liu, S. Zhuo, Z. Li, Y. Xie, H. J. Kim, N. L. Rosi and R. Jin, *ACS Nano*, 2016, **10**, 7998–8005.
71 S. Biswas, S. Das and Y. Negishi, *Nanoscale Horiz.*, 2023, **8**, 1509–1522.
72 H. Liang, B. J. Liu, B. Tang, S. C. Zhu, S. Li, X. Z. Ge, J. L. Li, J. R. Zhu and F. X. Xiao, *ACS Catal.*, 2022, **12**, 4216–4226.
73 P. Shen, S. Zhao, D. Su, Y. Li and A. Orlov, *Appl. Catal., B*, 2012, **126**, 153–160.
74 H. N. Kagalwala, E. Gottlieb, G. Li, T. Li, R. Jin and S. Bernhard, *Inorg. Chem.*, 2013, **52**, 9094–9101.
75 F. Tian, J. Chen, F. Chen, Y. Liu, Y. Xu and R. Chen, *Appl. Catal., B*, 2021, **292**, 120158.
76 F. Tian, X. Huang, W. Li, Y. An, G. Li and R. Chen, *ACS Catal.*, 2023, **13**, 12186–12196.
77 Y. D. Cao, H. P. Hao, H. S. Liu, D. Yin, M. L. Wang, G. G. Gao, L. L. Fan and H. Liu, *Nanoscale*, 2021, **13**, 16182–16188.
78 Y. Xu, Q. G. Dong, J. P. Dong, H. Zhang, B. Li, R. Wang and S. Q. Zang, *Chem. Commun.*, 2023, **59**, 3067–3070.
79 H. Wang, X. Zhang, W. Zhang, M. Zhou and H. L. Jiang, *Angew. Chem., Int. Ed.*, 2024, **63**, e202401443.
80 Y. D. Cao, D. Yin, S. Li, X. Y. Dong, Y. Feng, H. Liu, L. L. Fan, G. G. Gao and S. Q. Zang, *Angew. Chem., Int. Ed.*, 2023, **62**, e202307678.
81 X. Yan, X. Y. Fu and F. X. Xiao, *Adv. Funct. Mater.*, 2023, **33**, 2303737.
82 A. Yao, Y. Du, M. Han, Y. Wang, J. Hu, Q. Zhu, H. Sheng and M. Zhu, *Nano Res.*, 2022, **16**, 1527–1532.
83 C. Wang, P. Lv, D. Xue, Y. Cai, X. Yan, L. Xu, J. Fang and Y. Yang, *ACS Sustainable Chem. Eng.*, 2018, **6**, 8447–8457.
84 W. Kurashige, R. Hayashi, K. Wakamatsu, Y. Kataoka, S. Hossain, A. Iwase, A. Kudo, S. Yamazoe and Y. Negishi, *ACS Appl. Energy Mater.*, 2019, **2**, 4175–4187.
85 Y. Negishi, M. Mizuno, M. Hirayama, M. Omatoi, T. Takayama, A. Iwase and A. Kudo, *Nanoscale*, 2013, **5**, 7188–7192.
86 H. Mousavi, T. D. Small, S. K. Sharma, V. B. Golovko, C. J. Shearer and G. F. Metha, *Nanomaterials*, 2022, **12**, 3638.
87 W. Kurashige, R. Kumazawa, D. Ishii, R. Hayashi, Y. Niihori, S. Hossain, L. V. Nair, T. Takayama, A. Iwase, S. Yamazoe, T. Tsukuda, A. Kudo and Y. Negishi, *J. Phys. Chem. C*, 2018, **122**, 13669–13681.

This journal is © The Royal Society of Chemistry 2024